PHYSICAL REVIEW E **68**, 036402 (2003)

X-ray spectral measurements and collisional radiative modeling of Ni- to Kr-like Au ions in electron beam ion trap plasmas

M. J. May, K. B. Fournier, P. Beiersdorfer, H. Chen, and K. L. Wong
Lawrence Livermore National Laboratory, P.O. Box 808 L260, Livermore, California 94551, USA

(Received 23 April 2003; published 19 September 2003)

The line emission of $n=7\rightarrow3$, $6\rightarrow3$, $5\rightarrow3$, and $4\rightarrow3$ transitions in Ni- to Kr-like gold ions produced in the Livermore electron beam ion traps EBIT-I and EBIT-II has been recorded with an x-ray crystal spectrometer and a photometrically calibrated microcalorimeter. The plasmas had either monoenergetic electron beams with $E_{\mathrm{beam}}=2.66$, 3.53, or 4.54 keV or an experimentally simulated thermal electron distributions with $T_{\mathrm{e}}=2.5$ keV. The electron densities were $\approx10^{12}\mathrm{cm}^{-3}$. The measured spectra have been compared to atomic structure calculations and synthetic spectra provided by the Hebrew University Lawrence Livermore Atomic Code atomic data package. Line identifications and accurate photon energy measurements have been made for many collisionally excited transitions. Approximately 140 lines have been identified in nine charge states. Agreement within 20–30 % exists between the measured and modeled line intensities for most lines excited by the monoenergetic electron beam plasmas, although some larger discrepancies can be found for some weaker features.

DOI: 10.1103/PhysRevE.68.036402 PACS number(s): 52.20.Fs, 52.25.Jm, 34.70.+e, 34.80.Kw

I. INTRODUCTION

High temperature plasmas exist in Z pinches [1,2], tokamaks [3–5], astrophysical objects [6], and laser produced plasmas [7–9]. Important parameters such as radiation output, energy deposition rate, charge state distribution, energy balance, etc., must be correctly predicted to understand these plasmas. In indirect-drive inertially confined fusion (ICF) plasmas, laser radiation heats the inside of a gold hohlraum producing a plasma that emits intense x rays. The x-ray radiation drives the capsule implosion and influences the resulting fusion yield. Understanding the radiation drive requires the correct implementation of atomic physics in the modeling codes that are used to predict the intensity and photon energy of the Au x rays. Experiments must be done in a variety of conditions, not just those involving hohlraums, to provide the relevant atomic data and to test the modeling codes. For example, accurate measurements in low density plasmas of the photon energy of line emission can be used to correct the energy level structure calculated by atomic structure codes and to improve the calculated rates of the atomic physics processes used for the modeling of high density experiments. Also, emission line intensities measured in low density plasmas can be used to advance collisional radiative models and serve to select among the different approaches for calculating electron impact rates.

The need for controlled laboratory measurements that provide accurate atomic data is clear. Gold x-ray spectra in ICF relevant spectral regions have been previously studied by Kiyokawa *et al.* [10]. They recorded the $5f\rightarrow3d$ and $6f\rightarrow3d$ line groups from Ni- to Ga-like Au with E_{photon} of 3–4 keV from a laser heated gold disk. However, these line groups were misidentified as being composed of the $6d_{3/2}\rightarrow3p_{3/2}$ and $6d_{3/2}\rightarrow3p_{1/2}$ transitions. In later laser-produced plasma experiments, Bauche-Arnoult *et al.* [11] re-measured and correctly identified these line groups. In an experiment with the NOVA laser, Foord *et al.* [12] inferred the average charge state $\langle q\rangle$ of a gold plasma from the $5f\rightarrow3d$ lines in the Ni- to Kr-like ions. For this experiment, a gold microdot buried in a Be foil was laser heated to steady state conditions with $T_{\mathrm{e}}=2.2$ keV and $n_{\mathrm{e}}=6\times10^{20}$ cm^{-3}. The $\langle q\rangle$ of $+49.3$ was inferred by comparing the recorded spectrum with modeling from the Hebrew University Lawrence Livermore Atomic Code (HULLAC) [13]. Glenzer *et al.* [14] also measured a spectrum of the $5f\rightarrow3d$ lines emitted from a fusion hohlraum plasma with $T_{\mathrm{e}}=2.6$ keV, $n_{\mathrm{e}}=1.4\times10^{21}$ cm^{-3}, and $T_{\mathrm{rad}}=210$ eV and inferred a $\langle q\rangle$ of $+52\pm1$. Foord *et al.* and Glenzer *et al.* found reasonable agreement between the observed value of $\langle q\rangle$ and predictions from the plasma modeling code RIGEL [15]. However, the modeling of the spectral features in the high density experiments was challenging due to the many competing processes and effects (e.g., opacity, two-electron processes, photoionization, pressure broadening, etc.) and the transient nature of the experiment. Line identification and photon energy measurements were not possible due to the presence of unresolved transition arrays [11].

Here we present a systematic study of the emission from Ni- to Kr-like gold by using the plasmas of the Livermore electron beam ion traps EBIT-I and EBIT-II [16,17]. The gold plasmas were created with either a monoenergetic electron beam or an experimentally simulated thermal electron distribution. The line emission from the gold ions was observed in steady state at densities of $\approx10^{12}$ cm^{-3}. The plasmas at these densities have fewer active atomic physics processes and are more straightforward to model than the laser produced plasma experiments. Träbert *et al.* [18] used these plasmas to identify and to measure the photon energies of the $n=4\rightarrow4$ extreme ultraviolet (EUV) transitions between 30 and 60 Å from Cu- to Kr-like gold ions. In addition, the charge state distribution (CSD) of gold has been inferred for both the experimentally simulated thermal electron distribution and monoenergetic beam plasmas by comparing the measured spectra with HULLAC modeling [19,20].

1063-651X/2003/68(3)/036402(11)/$20.00

For this paper, we recorded the emission from $n=4\to3$, $5\to3$, $6\to3$, and $7\to3$ x-ray transitions from Ni- to Kr-like gold ions between 1500 and 5000 eV by employing both a photometrically calibrated x-ray microcalorimeter (XRS) [21] and an x-ray crystal spectrometer [22]. HULLAC was used to calculate the atomic structure and rates for comparisons with experiment. Approximately 140 emission lines between 1500 and 5000 eV have been identified, and accurate photon energy measurements have been made. Difference between the measured photon energies and HULLAC are as large as 20 eV, though many lines agree within a few eV. Synthetic spectra for plasmas with $E_{\mathrm{beam}}=3.53$ and 4.54 keV were generated by HULLAC and by using the CSD measurements in Ref. [20]. Agreement within 20–30 % exists between the XRS spectra and the HULLAC predictions for the more intense lines, although large discrepancies do exist for some of the weaker lines. In these low density plasmas the collisional excitation models for the Ni- to Ga-like charge states have been validated to this level of accuracy over a very broad photon energy range (1500–5000 eV). This analysis illustrates the limitations of modern spectral model calculations. The present analysis implies that HULLAC may provide spectra with similar accuracy for high density collisional plasmas, especially if the photon energies are corrected to the experimental values.

II. EXPERIMENT

Gold plasmas were produced in the electron beam ion traps EBIT-I and EBIT-II by successive electron collisional ionization of low-charged ions introduced into the trap from a metal vacuum vapor ion source [23]. Radial trapping of the ions in the electron mode [24] was achieved by the electrostatic attraction of the electron beam. Two end drift tubes, which have a positive bias of a few hundred volts with respect to a center drift tube, confined the ions axially along the beam. Plasmas produced by either a monoenergetic electron beam or an experimentally simulated thermal electron distribution were utilized to obtain the data presented here.

The monoenergetic electron beam plasmas created in EBIT-I had energies E_{beam} of 4.54 ± 0.04, 3.53 ± 0.04, and 2.66 ± 0.04 keV. The reported beam energies are corrected for the space charge effects of a beam current of ≈55 mA. The space charge V_{sp} (eV) is estimated to be $-2.5I_{\mathrm{beam}}$ (mA)/$\sqrt{E_{\mathrm{beam}}\,(\mathrm{keV})}$ [16]. The electron beam had a Gaussian electron energy distribution with a full width at half maximum of ≈50 eV. After entering the trap, the gold was ionized by the monoenergetic beam for ≈50 ms. The time history of the Au x-ray emission was monitored with a solid-state Ge detector to check when it came into steady state, which was after 1 sec. The ions were held in the trap by the monoenergetic beam for another 8 sec for the spectral measurements. The trap was then emptied by removing the voltage on the upper drift tube. For each of the beam energies, the trapping cycle was repeated for a total data acquisition time of ≈12 h during which time spectra were recorded. This time was necessary for the x-ray crystal spectrometer and the XRS to collect a sufficient number of counts. No XRS data were taken for the 2.66 keV plasma.

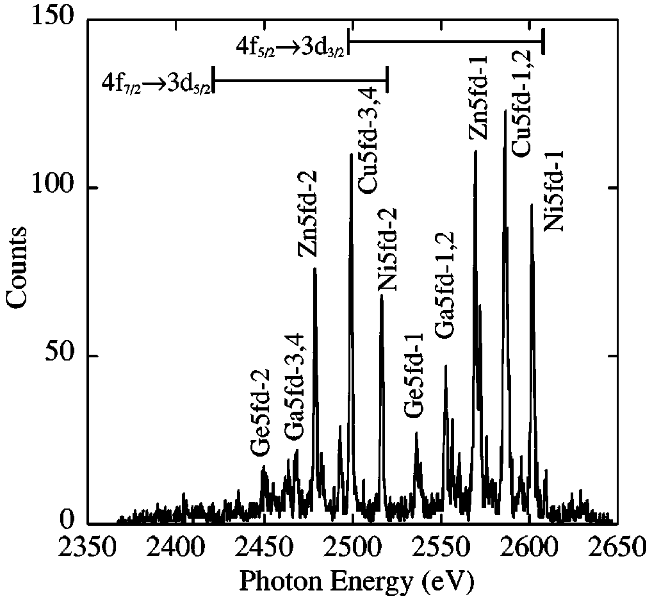

FIG. 1. Raw $4f\to3d$ spectrum at an electron beam energy of 3.53 keV recorded with the x-ray crystal spectrometer.

For the EBIT-II plasma with the experimentally simulated thermal electron distribution, the gold particles were initially ionized with a 2.2 keV monoenergetic electron beam for ≈50 ms after entering the trap. Then the electron beam energy and anode voltages were swept to map out a Maxwell-Boltzmann (MB) electron distribution in time with a temperature T_{e} of 2.50 ± 0.04 keV by using the techniques described in Ref. [25]. In each sweep, the time spent at an electron beam energy was proportional to the experimentally simulated temperature's Maxwell-Boltzmann electron distribution probability at that energy. The reported temperature includes the space charge correction for ≈41 mA of beam current. The beam energy was swept in 256 discrete voltage steps between electron energies of 0.2 eV and 12.5 keV. Concurrently, the anode voltage was swept to maintain a constant density in the electron beam. Each sweep, which lasted 5 ms, was continuously repeated until the end of the electron mode. Again, the Au x-ray emission was monitored and came into steady state after about 1 sec. The Au ions were held in the trap and interacted with the MB electron beam for another 6 sec during which time spectra were measured. The trapping cycle was repeated for ≈12 h until sufficient signal was recorded by the x-ray crystal spectrometer. The XRS was not installed on EBIT-II during the MB experiments.

The x-ray crystal spectrometer [22] recorded in first order the high-resolution spectra of the $n=5f\to3d$ and the $n=4f\to3d$ transitions of Ni- to Kr-like gold ions between photon energies of 3100 to 3500 eV and 2400 to 2600 eV, respectively. Sample raw spectra for plasmas with $E_{\mathrm{beam}}=3.53$ and 2.66 keV are shown in Figs. 1 and 2, respectively. The design of the x-ray crystal spectrometer accommodated two channels each having a separate crystal and gas flow proportional counter, which allowed both spectral ranges to be measured simultaneously. For these measurements, two Si(111) crystals with lattice spacings of $2d=6.2712$ Å were used. The nominal Bragg angle was 36° for the $5f\to3d$

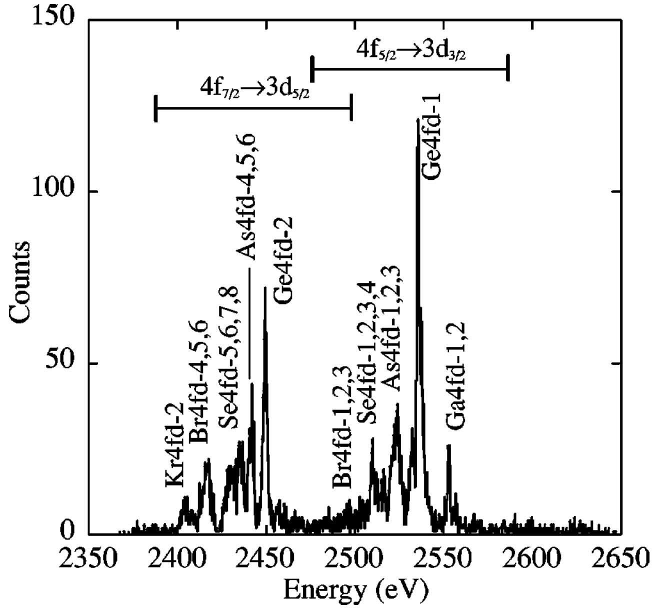

FIG. 2. Raw $n=4f\rightarrow 3d$ spectrum at an electron beam energy of 2.66 keV recorded with the x-ray crystal spectrometer.

transitions and 53° for the $4f\rightarrow 3d$ transitions. The x rays from each crystal were dispersed onto one of the two position-sensitive, gas flow proportional counters filled with ≈ 1 atm of $P10$ gas. The gas counter windows were either 4 μm of polypropylene or 1 μm of polyimide. In addition, each window was coated with a 100–200 Å Al layer. A vacuum isolation window composed of 0.5 μm of polyimide was located between the crystal spectrometer and EBIT-I or EBIT-II. The total energy coverage of each channel was ≈ 500 eV for the $5f\rightarrow 3d$ and ≈ 300 eV for the $4f\rightarrow 3d$ transitions. The energy resolution was ≈ 5.0 eV at 3300 eV and ≈ 2.5 eV at 2500 eV. A sharp falloff in the efficiency in the higher energy spectrum occurred below 3210 eV due to the Ar K absorption edge in the $P10$ gas. The lower energy region did not have any $P10$ absorption edges. The absorption of the gas and the transmission efficiency of the windows were taken into account when the experimental spectrum was compared with the modeling.

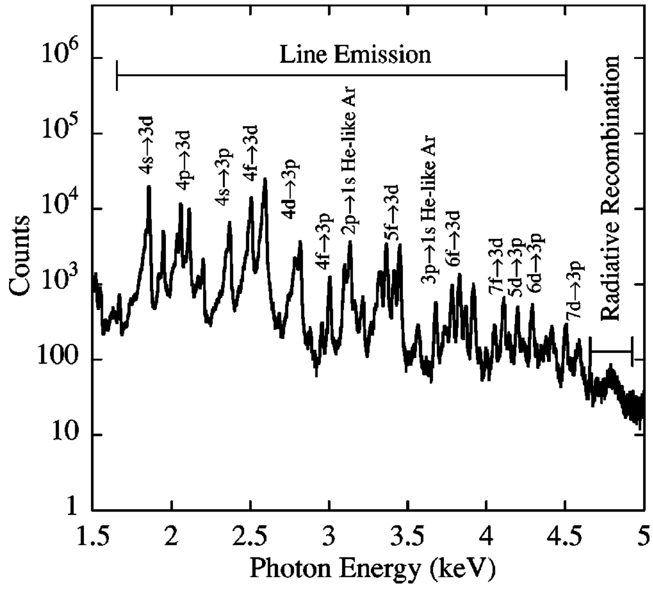

FIG. 3. Raw XRS spectrum in a plasma having E_{beam} of 4.54 keV.

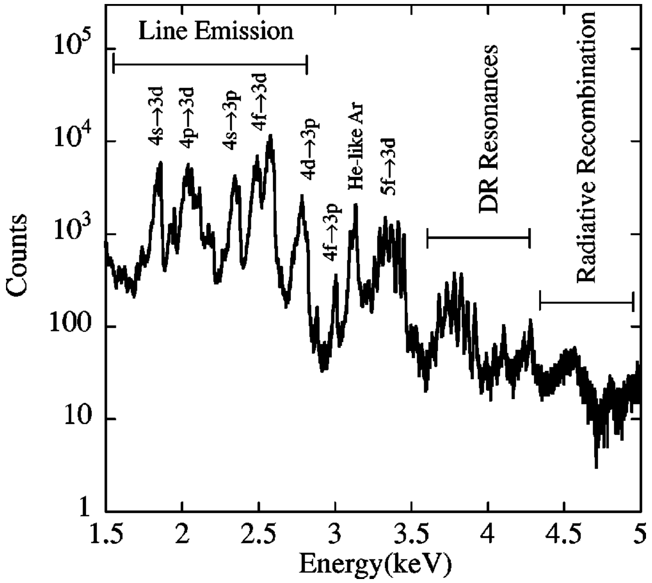

FIG. 4. Raw XRS spectrum in a plasma having E_{beam} of 3.53 keV.

The XRS microcalorimeter [21] recorded gold spectra between 1500 and 7500 eV. It was used to determine the photon energies for the spectral regions not covered by the crystal spectrometer and to measure absolute line intensities. Sample raw spectra are shown in Figs. 3 and 4 for $E_{\mathrm{beam}}=4.54$ and 3.53 keV, respectively. The XRS at our facility is the engineering version of the NASA Goddard Space Flight Center microcalorimeter flown on Astro-E [26], which failed to reach orbit. The XRS detector head consisted of an array of 36 ion-implanted thermistors (30 active) with a 8.5-μm thick HgTe photon absorber that had a total effective area of 12.5 mm^2. The thermistors directly measured the temperature change of a single photon absorbed by the HgTe. A spectrum can be extracted from the thermistor data since the change in temperature caused by a photon absorption is proportional to the photon energy. To measure the small changes in temperature, the detector head was cooled to an operating temperature of 59 mK by an adiabatic demagnetization refrigerator mounted inside a Dewar filled with superfluid helium. Since each absorber-thermistor must be recooled after each photon event, the maximum count rate was limited to ≈ 100 counts per second across the entire array. This count rate is well suited for astrophysical observations. The photon fluxes from EBIT-I and EBIT-II plasmas are typically very low. However, to keep the total flux onto the XRS below the saturation point, the beam current was kept below 60 mA. The width of the observed lines was ≈ 12 eV. This was slightly larger than the 10 eV nominal resolution of the XRS and may be the results of small instrumental drifts during the 12 h integration times.

A filter stack was located at the entrance of the XRS

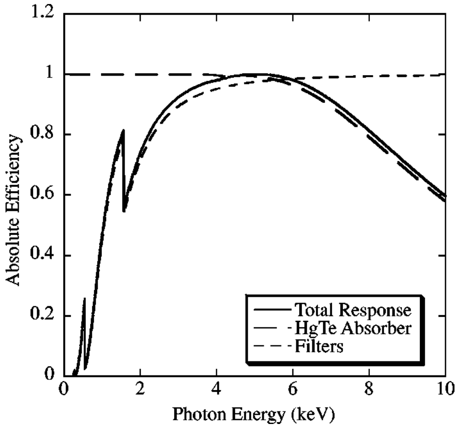

FIG. 5. Photometric response of the XRS.

which isolated its vacuum from that of the plasma and reduced the thermal loading on the Dewar. The filter stack consisted of five thin foil filters (four Al/polyimide with thicknesses of 545 Å/795 Å, 1023 Å/1045 Å, 1023 Å/1085 Å, 1023 Å/1085 Å, and 200 Å/1000 Å). The photometric response of the XRS has been determined [27,28] and was applied to the raw spectra for comparison with the HULLAC modeling. The photometric response (Fig. 5) included both the transmissions of the filters (short dashed line) and the absorption of the HgTe (long dashed lines). The K absorption edges of O and Al at 525 eV and 1480 eV, respectively, are seen in the filter transmission curve. The HgTe absorption efficiency was $>95\%$ for photons that had less than 6 keV of energy. At the higher photon energies, the absorption efficiency in the HgTe dropped to $\leqslant 75\%$ at 8 keV.

III. PHOTON ENERGY CALIBRATIONS

For the x-ray crystal spectrometer, the photon energy calibration of each crystal-proportional counter channel was determined separately from well-known calibration lines. For the 3100–3500 eV range, the calibration lines used were the $2p \rightarrow 1s$ Ly-$\alpha_{1,2}$ transitions in H-like argon and the $1s2p \rightarrow 1s^2$ $({}^1P_1 \rightarrow {}^1S_0)$, $1s2p \rightarrow 1s^2$ $({}^3P_1 \rightarrow {}^1S_0)$, and $1s2s \rightarrow 1s^2$ $({}^3S_1 \rightarrow {}^1S_0)$ resonance, intercombination, and forbidden lines in He-like argon. The equivalent H-like and He-like transitions of sulfur from SF_6 gas were used to calibrate the 2400 to 2600 eV region. These calibration lines have been calculated with much higher accuracy than the uncertainty in our measurements [29,30]. The gases Ar and SF_6 were introduced into the plasma by using a gas injector that had a continuous flow. The calibration spectra were measured in plasmas with constant electron beam energies of 4.4 keV for Ar and 3.7 keV for SF_6, without gold being injected into the trap.

The calibration lines measured by each crystal-detector channel were fit with a Gaussian line profile to determine their central channel number x_c. Each central channel number corresponded to a Bragg angle θ_c and a photon wavelength λ_c through the Bragg dispersion equation. A linear fit was performed on the calibration points to relate θ_{Bragg} to channel number x for each crystal-detector channel. The fit was inserted into the Bragg equation to obtain the wavelength

$$n\lambda(\text{Å}) = 2d\sin(\theta_{\mathrm{Bragg}}) = 2d\sin(mx+b).$$

The variables m and b are the fitting coefficients. The photon energy for each crystal-detector channel was obtained from $E_{\mathrm{photon}}(\mathrm{eV}) = 12\,398.42/\lambda(\text{Å})$. The profile of each Au line was fit with a Gaussian function to determine its central channel number and intensity. The photon energy of each line was obtained from the appropriate calibration. The experimental error on each measured energy included the uncertainty in determining the centroid of the calibration and the gold lines and the uncertainty in the fit of each energy dispersion. The measured photon energies for the $4f \rightarrow 3d$ and $5f \rightarrow 3d$ transitions are listed in Table I with the uncertainties on the measurements given in parenthesis after the photon energies.

The photon energy calibration of the XRS was determined between 300 and 7800 eV by also using a set of well-known calibration lines. These lines were the $2p \rightarrow 1s$ Ly-$\alpha_{1,2}$ transitions in H-like C, N, O, Ar, and Fe and the $1s2p \rightarrow 1s^2$ $({}^1P_1 \rightarrow {}^1S_0)$, $1s2p \rightarrow 1s^2$ $({}^3P_1 \rightarrow {}^1S_0)$, and $1s2s \rightarrow 1s^2$ $({}^3S_1 \rightarrow {}^1S_0)$ resonance, intercombination, and forbidden lines in He-like N, Ar, and Fe. In addition, the $1s3p \rightarrow 1s^2$ $({}^1P_1 \rightarrow {}^1S_0)$ line of He-like Fe was also used. Nitrogen and argon gas were injected into the trap for the calibration measurements. Carbon and oxygen were present as background ions in the trap. Iron was introduced into a plasma having a beam energy of 8.1 keV by using the metal vacuum vapor ion source.

The photon energy calibration of each of the 30 pixels of the XRS was determined separately. The central channel of each calibration line was determined from a Gaussian line fit. The photon energy versus channel number data for each pixel was fit with a fourth order polynomial. Each XRS pixel had a slightly different fit and photon energy calibration. The final XRS spectrum was the sum of all the pixel measurements after the application of the polynomial fits. The photon energy and intensity of each Au line was obtained from a Gaussian fit to the final XRS spectrum. For blended lines, each feature was fit with as many Gaussians as necessary to get a good fit. For some features, especially below 3000 eV (e.g., Zn4sd-1), it was impossible to determine individual lines even with a sufficient number of Gaussians in the fit. Consequently, these features were considered to be one ‘‘line’’ with an average photon energy and a total intensity. The measured photon energies are listed in Table I. The measurements of the $4 \rightarrow 3$ and $5 \rightarrow 3$ and Ni4pd-1 transitions with the XRS are not given since the crystal spectrometer provided more accurate photon energies.

The error on each photon energy included the uncertainty in determining the centroid of the calibration and the gold lines, the line blending, the uncertainty in the energy dispersion, and the accuracy of the polynomial fit. For the very blended features below 3000 eV, the uncertainties were determined from the widths of the total line feature. The errors (in eV) in the energy dispersion resulted from drifts in the

TABLE I. Au wavelength identifications of the $n=4\rightarrow3$, $5\rightarrow3$, $6\rightarrow3$, and $7\rightarrow3$ transitions measured with the XRS and x-ray crystal spectrometers. Column 1 contains a label given to each line, which includes the isoelectronic sequence, n and ℓ of the upper level, ℓ of the lower level, and a unique number for each line. Errors on the experimental photon energies in eV are given in the parenthesis. "b" signifies a blended line. "u" signifies an unidentified line.

Label	Charge state	Instrument	$E_{\text{Experiment}}$ (eV)	E_{HULLAC} (eV)	$E_{\text{Experiment}}$-E_{HUL}	J_{Upper}-J_{Lower}	Transition
Ga4sd-1	Au^{48+}	XRS	1798.8 (4.0)	1798.34	0.46	$\frac{5}{2}$-$\frac{1}{2}$	$3p^{6}3d^{4}_{3/2}3d^{5}_{5/2}4p^{2}_{1/2}\text{-}3p^{6}3d^{10}4s4p^{2}_{1/2}$
Zn4sd-3	Au^{49+}	XRS	1812.9 (4.0)	1818.75	−5.9	2-1	$3p^{6}3d^{4}_{3/2}3d^{5}_{5/2}4s^{2}4p_{1/2}\text{-}3p^{6}3d^{10}4s4p_{1/2}$
Zn4sd-3	Au^{49+}	XRS	b	1819.81	−6.9	3-1	$3p^{6}3d^{4}_{3/2}3d^{5}_{5/2}4s^{2}4p_{1/2}\text{-}3p^{6}3d^{10}4s4p_{1/2}$
Zn4sd-2	Au^{49+}	XRS	b	1826.92	0.58	2 - 0	$3p^{6}3d^{4}_{3/2}3d^{5}_{5/2}4s^{2}4p_{1/2}\text{-}3p^{6}3d^{10}4s4p_{1/2}$
Zn4sd-2	Au^{49+}	XRS	1827.5 (4.0)	1827.38	0.12	4-2	$3p^{6}3d^{4}_{3/2}3d^{5}_{5/2}4s^{2}4p_{3/2}\text{-}3p^{6}3d^{10}4s4p_{3/2}$
Cu4sd-3	Au^{50+}	XRS	1843.9 (1.6)	1842.23	1.7	$\frac{5}{2}$-$\frac{1}{2}$	$3p^{6}3d^{4}_{3/2}3d^{5}_{5/2}4s^{2}\text{-}3p^{6}3d^{10}4s$
Ni4sd-1	Au^{51+}	XRS	1862.8 (1.6)	1860.84	2.0	2-0	$3p^{6}3d^{4}_{3/2}3d^{5}_{5/2}4s\text{-}3p^{6}3d^{10}$
Zn4sd-1	Au^{49+}	XRS	1917.6 (6.0)	1909.35	8.3	2-1	$3p^{6}3d^{3}_{3/2}3d^{6}_{5/2}4s^{2}4p_{1/2}\text{-}3p^{6}3d^{10}4s4p_{1/2}$
Zn4sd-1	Au^{49+}	XRS	b	1914.90	2.7	0-2	$3p^{6}3d^{3}_{3/2}3d^{6}_{5/2}4s^{2}4p_{3/2}\text{-}3p^{6}3d^{10}4s4p_{3/2}$
Zn4sd-1	Au^{49+}	XRS	b	1917.53	0.07	2-0	$3p^{6}3d^{3}_{3/2}3d^{6}_{5/2}4s^{2}4p_{1/2}\text{-}3p^{6}3d^{10}4s4p_{1/2}$
Zn4sd-1	Au^{49+}	XRS	b	1919.88	−2.3	3-2	$3p^{6}3d^{3}_{3/2}3d^{6}_{5/2}4s^{2}4p_{3/2}\text{-}3p^{6}3d^{10}4s4p_{3/2}$
Zn4sd-1	Au^{49+}	XRS	b	1922.74	−5.1	2-2	$3p^{6}3d^{3}_{3/2}3d^{6}_{5/2}4s^{2}4p_{3/2}\text{-}3p^{6}3d^{10}4s4p_{3/2}$
Cu4sd-2	Au^{50+}	XRS	1933.4 (4.0)	1933.44	−0.04	$\frac{3}{2}$-$\frac{1}{2}$	$3p^{6}3d^{3}_{3/2}3d^{6}_{5/2}4s^{2}\text{-}3p^{6}3d^{10}4s$
Ni4pd-6	Au^{51+}	XRS	1954.1 (1.6)	1951.43	2.7	2-0	$3p^{6}3d^{3}_{3/2}3d^{6}_{5/2}4s\text{-}3p^{6}3d^{10}$
Ga4pd-1	Au^{48+}	XRS	2002.9 (4.0)	2001.19	1.7	$\frac{3}{2}$-$\frac{1}{2}$	$3p^{6}3d^{3}_{3/2}3d^{6}_{5/2}4p^{2}_{1/2}\text{-}3p^{6}3d^{10}4p_{1/2}$
Zn4pd-3	Au^{49+}	XRS	2024.2 (1.6)	2019.77	4.4	1-0	$3p^{6}3d^{3}_{3/2}3d^{6}_{5/2}4s^{2}4p_{1/2}\text{-}3p^{6}3d^{10}4s^{2}$
Cu4pd-6	Au^{50+}	XRS	2042.9 (1.6)	2039.08	3.8	$\frac{3}{2}$-$\frac{1}{2}$	$3p^{6}3d^{3}_{3/2}3d^{6}_{5/2}4s4p_{1/2}\text{-}3p^{6}3d^{10}4s$
Cu4pd-6	Au^{50+}	XRS	b	2040.02	2.9	$\frac{1}{2}$-$\frac{1}{2}$	$3p^{6}3d^{3}_{3/2}3d^{6}_{5/2}4s4p_{1/2}\text{-}3p^{6}3d^{10}4s$
Ni4pd-5	Au^{51+}	XRS	2066.0 (1.6)	2063.65	2.4	1-0	$3p^{6}3d^{3}_{3/2}3d^{6}_{5/2}4p_{1/2}\text{-}3p^{6}3d^{10}$
Zn4pd-2	Au^{49+}	XRS	u	2071.13		1 - 0	$3p^{6}3d^{4}_{3/2}3d^{5}_{5/2}4s^{2}4p_{3/2}\text{-}3p^{6}3d^{10}4s^{2}$
Cu4pd-5	Au^{50+}	XRS	b	2084.60	3.4	$\frac{3}{2}$-$\frac{1}{2}$	$3p^{6}3d^{4}_{3/2}3d^{5}_{5/2}4s4p_{3/2}\text{-}3p^{6}3d^{10}4s$
Cu4pd-5	Au^{50+}	XRS	2088.0 (1.6)	2085.76	2.2	$\frac{1}{2}$-$\frac{1}{2}$	$3p^{6}3d^{4}_{3/2}3d^{5}_{5/2}4s4p_{3/2}\text{-}3p^{6}3d^{10}4s$
Cu4pd-4	Au^{50+}	XRS	2102.1 (1.6)	2102.84	−0.74	$\frac{3}{2}$-$\frac{1}{2}$	$3p^{6}3d^{4}_{3/2}3d^{5}_{5/2}4s4p_{3/2}\text{-}3p^{6}3d^{10}4s$
Ni4pd-4	Au^{51+}	XRS	2118.6 (1.6)	2117.28	1.3	1-0	$3p^{6}3d^{4}_{3/2}3d^{5}_{5/2}4p_{3/2}\text{-}3p^{6}3d^{10}$
Cu4sd-1	Au^{50+}	XRS	2140.4 (4.0)	2141.86	−1.5	$\frac{1}{2}$-$\frac{3}{2}$	$3p^{6}3d^{3}_{3/2}3d^{6}_{5/2}4s4d_{3/2}\text{-}3p^{6}3d^{10}4p_{3/2}$
Zn4pd-1	Au^{49+}	XRS	2159.8 (4.0)	2159.66	0.14	1-0	$3p^{6}3d^{3}_{3/2}3d^{6}_{5/2}4s^{2}4p_{3/2}\text{-}3p^{6}3d^{10}4s^{2}$
Cu4pd-3	Au^{50+}	XRS	u	2169.52		$\frac{1}{2}$-$\frac{1}{2}$	$3p^{6}3d^{3}_{3/2}3d^{6}_{5/2}4s4p_{3/2}\text{-}3p^{6}3d^{10}4s$
Cu4pd-2	Au^{50+}	XRS	2176.2 (3.0)	2173.74	2.5	$\frac{3}{2}$-$\frac{1}{2}$	$3p^{6}3d^{3}_{3/2}3d^{6}_{5/2}4s4p_{3/2}\text{-}3p^{6}3d^{10}4s$
Cu4pd-1	Au^{50+}	XRS	2187.9 (3.0)	2192.23	−4.3	$\frac{1}{2}$-$\frac{1}{2}$	$3p^{6}3d^{3}_{3/2}3d^{6}_{5/2}4s4p_{3/2}\text{-}3p^{6}3d^{10}4s$
Ni4pd-3	Au^{51+}	XRS	2205.0 (1.6)	2206.51	−1.5	1 - 0	$3p^{6}3d^{3}_{3/2}3d^{6}_{5/2}4p_{3/2}\text{-}3p^{6}3d^{10}$
Ga4sp-1	Au^{48+}	XRS	u	2334.87		$\frac{1}{2}$-$\frac{3}{2}$	$3p^{2}_{1/2}3p^{3}_{3/2}3d^{10}4p_{1/2}4p_{3/2}\text{-}3p^{6}3d^{10}4s4p_{1/2}4p_{3/2}$
Zn4sp-2	Au^{49+}	XRS	b	2348.53	−12.1	2 - 3	$3p^{2}_{1/2}3p^{3}_{3/2}3d^{10}4s^{2}4f_{7/2}\text{-}3p^{6}3d^{10}4s4f_{7/2}$
Zn4sp-2	Au^{49+}	XRS	2336.4 (3.0)	2354.23	−17.8	0-1	$3p^{2}_{1/2}3p^{3}_{3/2}3d^{10}4s^{2}4p_{3/2}\text{-}3p^{6}3d^{10}4s4p_{3/2}$
Cu4sp-3	Au^{50+}	XRS	2350.0 (3.0)	2361.19	−10.2	$\frac{3}{2}$-$\frac{1}{2}$	$3p^{2}_{1/2}3p^{3}_{3/2}3d^{10}4s^{2}\text{-}3p^{6}3d^{10}4s$
Cu4sp-3	Au^{50+}	XRS	b	2362.81	−12.8	$\frac{5}{2}$-$\frac{7}{2}$	$3p^{2}_{1/2}3p^{3}_{3/2}3d^{10}4s4f_{7/2}\text{-}3p^{6}3d^{10}4f_{7/2}$
Ni4sp-1	Au^{51+}	XRS	2375.9 (1.6)	2377.58	−1.7	1-0	$3p^{2}_{1/2}3p^{3}_{3/2}3d^{10}4s\text{-}3p^{6}3d^{10}$
Cu4sp-2	Au^{50+}	XRS	2376.1 (1.6)	2380.73	−4.6	$\frac{1}{2}$-$\frac{3}{2}$	$3p^{2}_{1/2}3p^{3}_{3/2}3d^{10}4s4p_{3/2}\text{-}3p^{6}3d^{10}4p_{3/2}$
Kr4fd-2	Au^{43+}	crystal	2395.4 (0.5)	2398.97	−3.6	1-0	$3d^{4}_{3/2}3d^{5}_{5/2}4p^{6}4f_{7/2}\text{-}3d^{10}4p^{6}$
Br4fd-6	Au^{44+}	crystal	2414.8 (0.5)	2415.00	−0.2	$\frac{5}{2}$-$\frac{3}{2}$	$3d^{4}_{3/2}3d^{5}_{5/2}4p^{2}_{1/2}4p^{3}_{3/2}4f_{7/2}\text{-}3d^{10}4p^{2}_{1/2}4p^{3}_{3/2}$
Br4fd-5	Au^{44+}	crystal	2417.2 (0.5)	2415.38	1.8	$\frac{1}{2}$-$\frac{3}{2}$	$3d^{4}_{3/2}3d^{5}_{5/2}4p^{2}_{1/2}4p^{3}_{3/2}4f_{7/2}\text{-}3d^{10}4p^{2}_{1/2}4p^{3}_{3/2}$
Br4fd-4	Au^{44+}	crystal	2410.1 (0.5)	2417.54	−7.4	$\frac{3}{2}$-$\frac{3}{2}$	$3d^{4}_{3/2}3d^{5}_{5/2}4p^{2}_{1/2}4p^{3}_{3/2}4f_{7/2}\text{-}3d^{10}4p^{2}_{1/2}4p^{3}_{3/2}$
Se4fd-8	Au^{45+}	crystal	2423.4 (0.5)	2428.10	−4.7	1-0	$3d^{4}_{3/2}3d^{5}_{5/2}4p^{2}_{1/2}4p^{2}_{3/2}4f_{7/2}\text{-}3d^{10}4p^{2}_{1/2}4p^{2}_{3/2}$
Se4fd-7	Au^{45+}	crystal	2428.6 (0.5)	2428.77	−0.17	3-2	$3d^{4}_{3/2}3d^{5}_{5/2}4p_{1/2}4p^{3}_{3/2}4f_{5/2}\text{-}3d^{10}4p^{2}_{1/2}4p^{2}_{3/2}$
Se4fd-6	Au^{45+}	crystal	2430.1 (0.5)	2429.67	0.43	1-2	$3d^{4}_{3/2}3d^{5}_{5/2}4p^{2}_{1/2}4p^{2}_{3/2}4f_{7/2}\text{-}3d^{10}4p^{2}_{1/2}4p^{2}_{3/2}$
Se4fd-5	Au^{45+}	crystal	2427.0 (0.5)	2429.82	−2.8	2-2	$3d^{4}_{3/2}3d^{5}_{5/2}4p^{2}_{1/2}4p^{2}_{3/2}4f_{7/2}\text{-}3d^{10}4p^{2}_{1/2}4p^{2}_{3/2}$
As4fd-6	Au^{46+}	crystal	2439.4 (0.5)	2442.16	−2.8	$\frac{3}{2}$-$\frac{3}{2}$	$3d^{4}_{3/2}3d^{5}_{5/2}4p^{2}_{1/2}4p_{3/2}4f_{7/2}\text{-}3d^{10}4p^{2}_{1/2}4p_{3/2}$
As4fd-5	Au^{46+}	crystal	2441.1 (0.5)	2443.26	−2.2	$\frac{5}{2}$-$\frac{3}{2}$	$3d^{4}_{3/2}3d^{5}_{5/2}4p^{2}_{1/2}4p_{3/2}4f_{7/2}\text{-}3d^{10}4p^{2}_{1/2}4p_{3/2}$
As4fd-4	Au^{46+}	crystal	2435.8 (0.5)	2445.24	−9.4	$\frac{1}{2}$-$\frac{3}{2}$	$3d^{4}_{3/2}3d^{5}_{5/2}4p^{2}_{1/2}4p_{3/2}4f_{7/2}\text{-}3d^{10}4p^{2}_{1/2}4p_{3/2}$

TABLE I. (*Continued*).

Label	Charge state	Instrument	$E_{\mathrm{Experiment}}$ (eV)	E_{HULLAC} (eV)	$E_{\mathrm{Experiment}}$-E_{HUL}	J_{Upper}-J_{Lower}	Transition
Ge4fd-2	Au^{47+}	crystal	2450.5 (0.5)	2454.05	−3.6	1-0	$3d_{3/2}^{4}3d_{5/2}^{5}4p_{1/2}^{2}4f_{7/2}$-$3d^{10}4p_{1/2}^{2}$
Ga4fd-4	Au^{48+}	crystal	2463.2 (0.5)	2468.71	−5.5	$\frac{1}{2}$-$\frac{1}{2}$	$3d_{3/2}^{4}3d_{5/2}^{5}4p_{1/2}4f_{7/2}$-$3d^{10}4p_{1/2}$
Ga4fd-3	Au^{48+}	crystal	2469.1 (0.5)	2469.05	0.05	$\frac{3}{2}$-$\frac{1}{2}$	$3d_{3/2}^{4}3d_{5/2}^{5}4p_{1/2}4f_{7/2}$-$3d^{10}4p_{1/2}$
Zn4fd-2	Au^{49+}	crystal	2480.2 (0.5)	2485.09	−4.9	1-0	$3d_{3/2}^{4}3d_{5/2}^{5}4s^{2}4f_{7/2}$-$3d^{10}4s^{2}$
Kr4fd-1	Au^{43+}	crystal	u	2485.17		1-0	$3d_{3/2}^{3}3d_{5/2}^{6}4p^{6}4f_{5/2}$-$3d^{10}4p^{6}$
Cu4fd-4	Au^{50+}	crystal	b	2496.40	5.5	$\frac{1}{2}$-$\frac{1}{2}$	$3d_{3/2}^{4}3d_{5/2}^{5}4s4f_{7/2}$-$3d^{10}4s$
Cu4fd-3	Au^{50+}	crystal	2501.9 (0.5)	2496.70	5.2	$\frac{3}{2}$-$\frac{1}{2}$	$3d_{3/2}^{4}3d_{5/2}^{5}4s4f_{7/2}$-$3d^{10}4s$
Br4fd-3	Au^{44+}	crystal	2495.9 (0.5)	2500.93	−5.0	$\frac{1}{2}$-$\frac{3}{2}$	$3d_{3/2}^{3}3d_{5/2}^{6}4p_{1/2}^{2}4p_{3/2}^{3}4f_{5/2}$-$3d^{10}4p_{1/2}^{2}4p_{3/2}^{3}$
Br4fd-2	Au^{44+}	crystal	2498.9 (0.5)	2501.84	−2.9	$\frac{5}{2}$-$\frac{3}{2}$	$3d_{3/2}^{3}3d_{5/2}^{6}4p_{1/2}^{2}4p_{3/2}^{3}4f_{5/2}$-$3d^{10}4p_{1/2}^{2}4p_{3/2}^{3}$
Br4fd-1	Au^{44+}	crystal	2501.5 (0.5)	2503.61	−2.1	$\frac{3}{2}$-$\frac{3}{2}$	$3d_{3/2}^{3}3d_{5/2}^{6}4p_{1/2}^{2}4p_{3/2}^{3}4f_{5/2}$-$3d^{10}4p_{1/2}^{2}4p_{3/2}^{3}$
Ni4fd-2	Au^{51+}	crystal	2519.8 (0.5)	2512.84	7.0	1-0	$3d_{3/2}^{4}3d_{5/2}^{5}4f_{7/2}$-$3d^{10}$
Se4fd-4	Au^{45+}	crystal	2519.8 (0.5)	2514.58	5.2	1-0	$3d_{3/2}^{3}3d_{5/2}^{6}4p_{1/2}^{2}4p_{3/2}^{2}4f_{5/2}$-$3d^{10}4p_{1/2}^{2}4p_{3/2}^{2}$
Se4fd-3	Au^{45+}	crystal	2517.2 (0.5)	2514.78	2.4	1-2	$3d_{3/2}^{3}3d_{5/2}^{6}4p_{1/2}^{2}4p_{3/2}^{2}4f_{5/2}$-$3d^{10}4p_{1/2}^{2}4p_{3/2}^{2}$
Se4fd-2	Au^{45+}	crystal	2512.3 (0.5)	2516.16	−3.9	3-2	$3d_{3/2}^{3}3d_{5/2}^{6}4p_{1/2}^{2}4p_{3/2}^{2}4f_{5/2}$-$3d^{10}4p_{1/2}^{2}4p_{3/2}^{2}$
Se4fd-1	Au^{45+}	crystal	2514.8 (0.5)	2516.21	−1.4	2-2	$3d_{3/2}^{3}3d_{5/2}^{6}4p_{1/2}^{2}4p_{3/2}^{2}4f_{5/2}$-$3d^{10}4p_{1/2}^{2}4p_{3/2}^{2}$
As4fd-3	Au^{46+}	crystal	2530.3 (0.5)	2528.46	1.8	$\frac{3}{2}$-$\frac{3}{2}$	$3d_{3/2}^{3}3d_{5/2}^{6}4p_{1/2}^{2}4p_{3/2}4f_{5/2}$-$3d^{10}4p_{1/2}^{2}4p_{3/2}$
As4fd-2	Au^{46+}	crystal	2527.8 (0.5)	2530.58	−2.8	$\frac{1}{2}$-$\frac{3}{2}$	$3d_{3/2}^{3}3d_{5/2}^{6}4p_{1/2}^{2}4p_{3/2}4f_{5/2}$-$3d^{10}4p_{1/2}^{2}4p_{3/2}$
As4fd-1	Au^{46+}	crystal	2524.9 (0.5)	2530.68	−5.8	$\frac{5}{2}$-$\frac{3}{2}$	$3d_{3/2}^{3}3d_{5/2}^{6}4p_{1/2}^{2}4p_{3/2}4f_{5/2}$-$3d^{10}4p_{1/2}^{2}4p_{3/2}$
Ge4fd-1	Au^{47+}	crystal	2539.9 (0.5)	2541.11	−1.2	1-0	$3d_{3/2}^{3}3d_{5/2}^{6}4p_{1/2}^{2}4f_{5/2}$-$3d^{10}4p_{1/2}^{2}$
Ga4fd-2	Au^{48+}	crystal	2556.3 (0.5)	2555.78	0.52	$\frac{3}{2}$-$\frac{1}{2}$	$3d_{3/2}^{3}3d_{5/2}^{6}4p_{1/2}4f_{5/2}$-$3d^{10}4p_{1/2}$
Ga4fd-1	Au^{48+}	crystal	2560.1 (0.5)	2558.94	1.2	$\frac{1}{2}$-$\frac{1}{2}$	$3d_{3/2}^{3}3d_{5/2}^{6}4p_{1/2}4f_{5/2}$-$3d^{10}4p_{1/2}$
Zn4fd-1	Au^{49+}	crystal	2572.8 (0.5)	2574.03	−1.2	1-0	$3d_{3/2}^{3}3d_{5/2}^{6}4s^{2}4f_{5/2}$ - $3d^{10}4s^{2}$
Cu4fd-2	Au^{50+}	crystal	2588.3 (0.5)	2584.82	3.5	$\frac{1}{2}$-$\frac{1}{2}$	$3d_{3/2}^{3}3d_{5/2}^{6}4s4f_{5/2}$-$3d^{10}4s$
Cu4fd-1	Au^{50+}	crystal	2589.4 (0.5)	2586.60	2.8	$\frac{3}{2}$-$\frac{1}{2}$	$3d_{3/2}^{3}3d_{5/2}^{6}4s4f_{5/2}$-$3d^{10}4s$
Ni4fd-1	Au^{51+}	crystal	2603.6 (0.5)	2602.18	1.4	1-0	$3d_{3/2}^{3}3d_{5/2}^{6}4f_{5/2}$-$3d^{10}$
Zn4sp-1	Au^{49+}	XRS	2761.8 (3.0)	2772.68	−10.9	2-3	$3p_{1/2}3p_{3/2}^{4}3d^{10}4s^{2}4f_{5/2}$-$3p^{6}3d^{10}4s4f_{5/2}$
Ga4dp-1	Au^{48+}	XRS	b	2775.42	−13.6	$\frac{1}{2}$-$\frac{1}{2}$	$3p_{1/2}^{2}3p_{3/2}^{3}3d^{10}4p_{1/2}4d_{5/2}$-$3p^{6}3d^{10}4p_{1/2}$
Ga4dp-1	Au^{48+}	XRS	2751.2 (3.0)	2776.04	−24.8	$\frac{1}{2}$-$\frac{3}{2}$	$3p_{1/2}^{2}3p_{3/2}^{3}3d^{10}4p_{1/2}4d_{5/2}$-$3p^{6}3d^{10}4p_{1/2}$
Cu4sp-1	Au^{50+}	XRS	2790.6 (3.0)	2792.22	−1.6	$\frac{1}{2}$-$\frac{1}{2}$	$3p_{1/2}3p_{3/2}^{4}3d^{10}4s4p_{1/2}$-$3p^{6}3d^{10}4p_{1/2}$
Zn4dp-1	Au^{49+}	XRS	b	2794.05	−3.5	1-0	$3p_{1/2}^{2}3p_{3/2}^{3}3d^{10}4s^{2}4d_{5/2}$-$3p^{6}3d^{10}4s^{2}$
Cu4dp-3	Au^{50+}	XRS	2808.4 (3.0)	2807.21	1.2	$\frac{3}{2}$-$\frac{1}{2}$	$3p_{1/2}^{2}3p_{3/2}^{3}3d^{10}4sd_{5/2}$-$3p^{6}3d^{10}4s$
Cu4dp-2	Au^{50+}	XRS	b	2813.13	−4,7	$\frac{1}{2}$-$\frac{1}{2}$	$3p_{1/2}^{2}3p_{3/2}^{3}3d^{10}4s4d_{5/2}$-$3p^{6}3d^{10}4s$
Ni4dp-2	Au^{51+}	XRS	2825.5 (3.0)	2827.82	−2.3	1-0	$3p_{1/2}^{2}3p_{3/2}^{3}3d^{10}4d_{5/2}$-$3p^{6}3d^{10}$
Cu4fp-1	Au^{50+}	XRS	u	3000.34		$\frac{3}{2}$-$\frac{1}{2}$	$3p_{1/2}^{2}3p_{3/2}^{3}3d^{10}4s4f_{7/2}$-$3p^{6}3d^{10}4s$
Ni4fp-1	Au^{51+}	XRS	3012.4 (1.6)	3015.00	−2.6	2-0	$3p_{1/2}^{2}3p_{3/2}^{3}3d^{10}4f_{7/2}$-$3p^{6}3d^{10}$
Kr5fd-2	Au^{43+}	crystal	u	3100.39		1-0	$3d_{3/2}^{4}3d_{5/2}^{5}4p^{6}5f_{7/2}$-$3d^{10}4p^{6}$
Br5fd-6	Au^{44+}	crystal	u	3134.88		$\frac{1}{2}$-$\frac{3}{2}$	$3d_{3/2}^{4}3d_{5/2}^{5}4p_{1/2}^{2}4p_{3/2}^{3}5f_{7/2}$-$3d^{10}4p_{1/2}^{2}4p_{3/2}^{3}$
Br5fd-5	Au^{44+}	crystal	3131.9 (0.5)	3136.43	−4.5	$\frac{3}{2}$-$\frac{3}{2}$	$3d_{3/2}^{4}3d_{5/2}^{5}4p_{1/2}^{2}4p_{3/2}^{3}5f_{7/2}$-$3d^{10}4p_{1/2}^{2}4p_{3/2}^{3}$
Br5fd-4	Au^{44+}	crystal	u	3136.86		$\frac{5}{2}$-$\frac{3}{2}$	$3d_{3/2}^{4}3d_{5/2}^{5}4p_{1/2}^{2}4p_{3/2}^{3}5f_{7/2}$-$3d^{10}4p_{1/2}^{2}4p_{3/2}^{3}$
Se5fd-8	Au^{45+}	crystal	u	3167.14		1-0	$3d_{3/2}^{4}3d_{5/2}^{5}4p_{1/2}^{2}4p_{3/2}^{2}5f_{7/2}$-$3d^{10}4p_{1/2}^{2}4p_{3/2}^{2}$
Se5fd-7	Au^{45+}	crystal	3164.2 (0.6)	3167.27	−3.1	1-2	$3d_{3/2}^{4}3d_{5/2}^{5}4p_{1/2}^{2}4p_{3/2}^{2}5f_{7/2}$-$3d^{10}4p_{1/2}^{2}4p_{3/2}^{2}$
Se5fd-6	Au^{45+}	crystal	3179.8 (0.7)	3167.84	12.5	2-2	$3d_{3/2}^{4}3d_{5/2}^{5}4p_{1/2}^{2}4p_{3/2}^{2}5f_{7/2}$-$3d^{10}4p_{1/2}^{2}4p_{3/2}^{2}$
Se5fd-5	Au^{45+}	crystal	3167.3 (0.9)	3168.40	−1.1	3-2	$3d_{3/2}^{3}3d_{5/2}^{6}4p_{1/2}^{2}4p_{3/2}^{2}5f_{5/2}$-$3d^{10}4p_{1/2}^{2}4p_{3/2}^{2}$
Ni5pd-1	Au^{51+}	XRS	3173.3 (1.6)	3184.68	−11.4	1-0	$3p^{6}3d_{3/2}^{4}3d_{5/2}^{5}5p_{3/2}$-$3p^{6}3d^{10}$
Cu4dp-1	Au^{50+}	XRS	3205.4 (1.6)	3205.60	−0.2	$\frac{3}{2}$-$\frac{1}{2}$	$3p_{1/2}3p_{3/2}^{4}3d^{10}4s4d_{3/2}$-$3p^{6}3d^{10}4s$
Ni4dp-1	Au^{51+}	crystal	3226.7 (0.7)	3224.19	2.5	1-0	$3p_{1/2}3p_{3/2}^{4}3d^{10}4d_{3/2}$-$3p^{6}3d^{10}$
Kr5fd-1	Au^{43+}	crystal	u	3184.22		1-0	$3d_{3/2}^{3}3d_{5/2}^{6}4p^{6}5f_{5/2}$-$3d^{10}4p^{6}$
As5fd-6	Au^{46+}	crystal	u	3200.33		$\frac{3}{2}$-$\frac{3}{2}$	$3d_{3/2}^{4}3d_{5/2}^{5}4p_{1/2}^{2}4p_{3/2}5f_{7/2}$-$3d^{10}4p_{1/2}^{2}4p_{3/2}$
As5fd-5	Au^{46+}	crystal	3191.1 (0.7)	3200.96	−10.0	$\frac{1}{2}$-$\frac{3}{2}$	$3d_{3/2}^{4}3d_{5/2}^{5}4p_{1/2}^{2}4p_{3/2}5f_{7/2}$-$3d^{10}4p_{1/2}^{2}4p_{3/2}$
As5fd-4	Au^{46+}	crystal	3194.1 (0.5)	3201.71	−7.6	$\frac{5}{2}$-$\frac{3}{2}$	$3d_{3/2}^{4}3d_{5/2}^{5}4p_{1/2}4p_{3/2}^{2}5f_{7/2}$-$3d^{10}4p_{1/2}^{2}4p_{3/2}$

TABLE I. (*Continued*).

Label	Charge state	Instrument	$E_{\text{Experiment}}$ (eV)	E_{HULLAC} (eV)	$E_{\text{Experiment}}$-E_{HUL}	J_{Upper}-J_{Lower}	Transition
Br5fd-3	Au^{44+}	crystal	3213.9 (0.6)	3219.67	−5.8	$\frac{1}{2}$-$\frac{3}{2}$	$3d_{3/2}^{3}3d_{5/2}^{6}4p_{1/2}^{2}4p_{3/2}^{3}5f_{5/2}$-$3d^{10}4p_{1/2}^{2}4p_{3/2}^{3}$
Br5fd-2	Au^{44+}	crystal	3207.0 (0.5)	3220.25	−13.3	$\frac{5}{2}$-$\frac{3}{2}$	$3d_{3/2}^{3}3d_{5/2}^{6}4p_{1/2}^{2}4p_{3/2}^{3}5f_{5/2}$-$3d^{10}4p_{1/2}^{2}4p_{3/2}^{3}$
Br5fd-1	Au^{44+}	crystal	3211.2 (0.6)	3221.01	−9.8	$\frac{3}{2}$-$\frac{3}{2}$	$3d_{3/2}^{3}3d_{5/2}^{6}4p_{1/2}^{2}4p_{3/2}^{3}5f_{5/2}$-$3d^{10}4p_{1/2}^{2}4p_{3/2}^{3}$
Ge5fd-2	Au^{47+}	crystal	3226.5 (0.5)	3230.99	−4.5	1-0	$3d_{3/2}^{4}3d_{5/2}^{5}4p_{1/2}^{2}5f_{7/2}$-$3d^{10}4p_{1/2}^{2}$
Se5fd-4	Au^{45+}	crystal	u	3252.03		1-0	$3d_{3/2}^{3}3d_{5/2}^{6}4p_{1/2}^{2}4p_{3/2}^{2}5f_{5/2}$-$3d^{10}4p_{1/2}^{2}4p_{3/2}^{2}$
Se5fd-3	Au^{45+}	crystal	3241.9 (0.5)	3252.52	−10.6	3-2	$3d_{3/2}^{3}3d_{5/2}^{6}4p_{1/2}4p_{3/2}^{3}5f_{5/2}$-$3d^{10}4p_{1/2}^{2}4p_{3/2}^{2}$
Se5fd-2	Au^{45+}	crystal	3245.8 (0.5)	3252.77	−7.0	1-2	$3d_{3/2}^{3}3d_{5/2}^{6}4p_{1/2}^{2}4p_{3/2}^{2}5f_{5/2}$-$3d^{10}4p_{1/2}^{2}4p_{3/2}^{2}$
Se5fd-1	Au^{45+}	crystal	u	3252.97		2-2	$3d_{3/2}^{3}3d_{5/2}^{6}4p_{1/2}^{2}4p_{3/2}^{2}5f_{5/2}$-$3d^{10}4p_{1/2}^{2}4p_{3/2}^{2}$
Ga5fd-4	Au^{48+}	crystal	3259.9 (0.5)	3265.88	−6.0	$\frac{3}{2}$-$\frac{1}{2}$	$3d_{3/2}^{4}3d_{5/2}^{5}4p_{1/2}5f_{7/2}$-$3d^{10}4p_{1/2}$
Ga5fd-3	Au^{48+}	crystal	b	3266.31		$\frac{1}{2}$-$\frac{1}{2}$	$3d_{3/2}^{4}3d_{5/2}^{5}4p_{1/2}5f_{7/2}$-$3d^{10}4p_{1/2}$
As5fd-3	Au^{46+}	crystal	3273.7 (0.5)	3285.36	−11.7	$\frac{3}{2}$-$\frac{3}{2}$	$3d_{3/2}^{3}3d_{5/2}^{6}4p_{1/2}^{2}4p_{3/2}5f_{5/2}$-$3d^{10}4p_{1/2}^{2}4p_{3/2}$
As5fd-2	Au^{46+}	crystal	3276.8 (0.6)	3286.23	−9.4	$\frac{5}{2}$-$\frac{3}{2}$	$3d_{3/2}^{3}3d_{5/2}^{6}4p_{1/2}^{2}4p_{3/2}5f_{5/2}$-$3d^{10}4p_{1/2}^{2}4p_{3/2}$
As5fd-1	Au^{46+}	crystal	3283.7 (0.6)	3286.75	−3.1	$\frac{1}{2}$-$\frac{3}{2}$	$3d_{3/2}^{3}3d_{5/2}^{6}4p_{1/2}^{2}4p_{3/2}5f_{5/2}$-$3d^{10}4p_{1/2}^{2}4p_{3/2}$
Zn5fd-1	Au^{49+}	crystal	3296.6 (0.5)	3302.42	−5.8	1-0	$3d_{3/2}^{4}3d_{5/2}^{5}4s^{2}5f_{7/2}$-$3d^{10}4s^{2}$
Ge5fd-1	Au^{47+}	crystal	3312.2 (0.6)	3316.56	−4.4	1-0	$3d_{3/2}^{3}3d_{5/2}^{6}4p_{1/2}^{2}5f_{5/2}$-$3d^{10}4p_{1/2}^{2}$
Cu5fd-4	Au^{50+}	crystal	3333.2 (0.5)	3333.49	−0.29	$\frac{1}{2}$-$\frac{1}{2}$	$3d_{3/2}^{4}3d_{5/2}^{5}4s5f_{7/2}$-$3d^{10}4s$
Cu5fd-3	Au^{50+}	crystal	3334.7 (0.5)	3334.48	0.22	$\frac{3}{2}$-$\frac{1}{2}$	$3d_{3/2}^{4}3d_{5/2}^{5}4s5f_{7/2}$-$3d^{10}4s$
Ga5fd-2	Au^{48+}	crystal	3345.3 (0.6)	3350.34	−5.0	$\frac{1}{2}$-$\frac{1}{2}$	$3d_{3/2}^{3}3d_{5/2}^{6}4p_{1/2}5f_{5/2}$-$3d^{10}4p_{1/2}$
Ga5fd-1	Au^{48+}	crystal	3348.3 (0.5)	3351.70	−3.4	$\frac{3}{2}$-$\frac{1}{2}$	$3d_{3/2}^{3}3d_{5/2}^{6}4p_{1/2}5f_{5/2}$-$3d^{10}4p_{1/2}$
Ni5fd-2	Au^{51+}	crystal	3370.6 (0.5)	3370.93	−0.33	1-0	$3d_{3/2}^{4}3d_{5/2}^{5}5f_{7/2}$-$3d^{10}$
Zn5fd-1	Au^{49+}	crystal	3382.7 (0.5)	3387.14	−4.4	1-0	$3d_{3/2}^{3}3d_{5/2}^{6}4s^{2}5f_{5/2}$-$3d^{10}4s^{2}$
Cu5fd-2	Au^{50+}	crystal	3420.8 (0.6)	3419.07	1.7	$\frac{3}{2}$-$\frac{1}{2}$	$3d_{3/2}^{3}3d_{5/2}^{6}4s$ 5f$_{5/2}$-$3d^{10}4s$
Cu5fd-1	Au^{50+}	crystal	3426.2 (0.5)	3419.45	6.8	$\frac{1}{2}$-$\frac{1}{2}$	$3d_{3/2}^{3}3d_{5/2}^{6}4s5f_{5/2}$-$3d^{10}4s$
Ni5fd-1	Au^{51+}	crystal	3458.3 (0.5)	3455.86	2.4	1-0	$3d_{3/2}^{3}3d_{5/2}^{6}5f_{5/2}$-$3d^{10}$
Ni5sp-1	Au^{51+}	XRS	3575.2 (1.6)	3575.66	−0.46	1-0	$3p_{1/2}^{2}3p_{3/2}^{3}3d^{10}5s$-$3p^{6}3d^{10}$
Cu6fd-2	Au^{50+}	XRS	b	3787.56	0.44	$\frac{1}{2}$-$\frac{1}{2}$	$3p^{6}3d_{3/2}^{4}3d_{5/2}^{5}4s6f_{7/2}$-$3p^{6}3d^{10}4s$
Cu6fd-2	Au^{50+}	XRS	3788.0 (1.6)	3788.72	−0.72	$\frac{3}{2}$-$\frac{1}{2}$	$3p^{6}3d_{3/2}^{4}3d_{5/2}^{5}4s6f_{7/2}$-$3p^{6}3d^{10}4s$
Ni5dp-1	Au^{51+}	XRS	3792.0 (1.6)	3792.55	0.55	1-0	$3p_{1/2}^{2}3p_{3/2}^{3}3d^{10}5d_{5/2}$-$3p^{6}3d^{10}$
Ni6fd-2	Au^{51+}	XRS	3838.6 (1.6)	3836.44	2.2	1-0	$3p^{6}3d_{3/2}^{4}3d_{5/2}^{5}6f_{7/2}$-$3p^{6}3d^{10}$
Cu6fd-1	Au^{50+}	XRS	3878.3 (1.6)	3875.29	3.0	$\frac{3}{2}$-$\frac{1}{2}$	$3p^{6}3d_{3/2}^{3}3d_{5/2}^{6}4s6f_{5/2}$-$3p^{6}3d^{10}4s$
Cu6fd-1	Au^{50+}	XRS	b	3875.65		$\frac{1}{2}$-$\frac{1}{2}$	$3p^{6}3d_{3/2}^{3}3d_{5/2}^{6}4s6f_{5/2}$-$3p^{6}3d^{10}4s$
Ni6fd-1	Au^{51+}	XRS	3927.1 (1.6)	3923.36	3.7	1-0	$3p^{6}3d_{3/2}^{3}3d_{5/2}^{6}6f_{5/2}$-$3p^{6}3d^{10}$
Cu7fd-2	Au^{50+}	XRS	4059.5 (1.6)	4059.79	−0.29	$\frac{3}{2}$-$\frac{1}{2}$	$3p^{6}3d_{3/2}^{4}3d_{5/2}^{5}4s7f_{7/2}$-$3p^{6}3d^{10}4s$
Ni7fd-2	Au^{51+}	XRS	4118.7 (1.6)	4116.12	2.6	1-0	$3p^{6}3d_{3/2}^{4}3d_{5/2}^{5}7f_{7/2}$-$3p^{6}3d^{10}$
Cu7fd-1	Au^{50+}	XRS	4150.5 (1.6)	4147.80	2.7	$\frac{3}{2}$-$\frac{1}{2}$	$3p^{6}3d_{3/2}^{3}3d_{5/2}^{6}4s7f_{5/2}$-$3p^{6}3d^{10}4s$
Ni7fd-1	Au^{51+}	XRS	4208.3 (1.6)	4204.48	3.8	1-0	$3p^{6}3d_{3/2}^{3}3d_{5/2}^{6}7f_{5/2}$-$3p^{6}3d^{10}$
Ni5dp-1	Au^{51+}	XRS	b	4205.77	2.5	1-0	$3p_{1/2}3p_{3/2}^{4}3d^{10}5d_{3/2}$-$3p^{6}3d^{10}$
Cu8fd-1	Au^{50+}	XRS	4245.1 (1.6)	4235.07	10.0	$\frac{3}{2}$-$\frac{1}{2}$	$3p^{6}3d_{3/2}^{4}3d_{5/2}^{5}4s8f_{7/2}$-$3p^{6}3d^{10}4s$
Ni8fd-2	Au^{51+}	XRS	b	4297.01	4.8	1-0	$3p^{6}3d_{3/2}^{4}3d_{5/2}^{5}8f_{7/2}$-$3p^{6}3d^{10}$
Ni6dp-1	Au^{51+}	XRS	4301.8 (1.6)	4298.95	2.85	1-0	$3p_{1/2}^{2}3p_{3/2}^{3}3d^{10}6d_{5/2}$-$3p^{6}3d^{10}$
Ni8fd-1	Au^{51+}	XRS	4391.4 (1.6)	4386.71	4.7	1-0	$3p^{6}3d_{3/2}^{3}3d_{5/2}^{6}8f_{5/2}$-$3p^{6}3d^{10}$
Ni7dp-1	Au^{51+}	XRS	4599.5 (1.6)	4597.86	1.6	1-0	$3p_{1/2}^{2}3p_{3/2}^{3}3d^{10}7d_{5/2}$-$3p^{6}3d^{10}$

XRS electronics during the time period for each measurement. The uncertainties are shown in parenthesis after the photon energies.

IV. ATOMIC PHYSICS AND SPECTRAL MODELING

The HULLAC atomic data package [13] was used to calculate the atomic structure, transition rates, and synthetic line intensities for the Ni- to Kr-like Au ions. The HULLAC data were used to identify the measured transitions. Synthetic spectra were produced for detailed comparisons with the XRS spectra from the monoenergetic beam plasmas having $E_{\text{beam}} = 4.54$ and 3.53 keV. Detailed modeling of the experimentally simulated thermal plasmas is discussed in Refs. [19,20,31].

The radiative transition rates and energy level structure of

TABLE II. Charge state balance used for HULLAC modeling of EBIT-I plasmas with $E_{\mathrm{beam}}=3.53$ and 4.54 keV.

Ionization state	Ion fraction at 4.54 keV	Ion fraction at 3.53 keV
Au^{+51}	0.70	0.20
Au^{+50}	0.26	0.35
Au^{+49}	0.048	0.31
Au^{+48}		0.10
Au^{+47}		0.035

each ionization state were calculated from the Dirac equation with a parametric potential. Electron impact excitation cross sections σ were calculated semirelativistically in the distorted wave approximation. For the experimentally simulated thermal plasma, the final electron-impact excitation rate coefficients $Q=\langle\sigma v\rangle$ were obtained by integrating over a Maxwell-Boltzmann electron energy distribution. The variable v is the velocity of the electrons. For the monoenergetic electron beam plasmas, the effective electron impact rate coefficient was just σv at the beam energy of interest.

Due to the low electron density of the trapped ions, the modeling in this paper only addresses transitions that are fed primarily through collisional excitation from the ground level. Nevertheless, all possible $n=4\rightarrow4$ and $n=3\rightarrow4$ to $3\rightarrow7$ excitations to singly excited configurations were included for Ni- to Ga-like ions. The models for the Ge to Kr-like ions contained only the $n=4\rightarrow4$, $n=3\rightarrow4$, and $3\rightarrow5$ excitations. To create the Ge- to Kr-like ions required a beam energy of less than 3.0 keV, which is below the threshold for collisional excitation for the $n\geqslant6$ transitions. Therefore, these lines were not observed in the XRS spectra and were not modeled. The simpler ions such as Ni- and Kr-like gold included several hundred levels. The more complicated ions such as As-like gold had several thousand levels. The level populations of each ionization state were coupled with those of the adjacent, higher-charged ion. The model for the higher-charged ion included fewer levels than the lower-charged ion and was only considered to include the small effect of dielectronic recombination on the collisionally excited transitions. Dielectronic recombination rate coefficients were found by requiring detailed balance of the HULLAC autoionization rates. All electric and magnetic dipole and quadrupole radiative transitions ($E1$, $M1$, $E2$, and $M2$) were included. The rate coefficients and the radiative transition probabilities were put into a collisional-radiative matrix. The level populations were calculated by solving the coupled set of equations

$$\frac{dn_j}{dt}=0=\sum_i n_iR_{i\rightarrow j}-n_j\sum_i R_{j\rightarrow i},$$

where n_i is the relative population of level "i" of a given ion, $R_{j\rightarrow i}$ is the rate at which population transfers from level "j" to level "i," which can be in the adjacent ionization state. The relative emissivity $J_{i\rightarrow j}$ for each transition within an ionization state was calculated for either a Maxwell-Boltzmann temperature or a Gaussian electron distribution with $\Delta E_{\mathrm{FWHM}}=50$ eV.

The monoenergetic beam plasmas contained several charge states of gold. A charge state distribution was required to fully model each spectrum. HULLAC could not calculate an accurate CSD. Therefore, the CSDs were determined by independently scaling HULLAC intensities in each ionization state to each of the $5f\rightarrow3d$ and $4f\rightarrow3d$ spectral lines recorded by the crystal spectrometer. The average CSDs from both spectral bands were used to create a synthetic spectrum and are listed in Table II for the plasmas with $E_{\mathrm{beam}}=4.53$ and 3.63 keV. A detailed discussion of the CSD analysis and the crystal spectrometer calibration is presented in Ref. [20].

V. SPECTRAL LINE IDENTIFICATIONS

Many emission lines between 1500 and 5000 eV were identified in the XRS and crystal spectra in all four plasmas. Each plasma allowed us to isolate a specific set of gold ionization states in the trap. The highest monoenergetic beam plasma had $E_{\mathrm{beam}}=4.54$ keV, which is near the calculated ionization threshold of Ni-like gold at 4.89 keV [32] but well above the threshold to ionize Cu-like into Ni-like at 2.96 keV. Therefore, Ni-like Au was the dominant ion in the trap and produced the most intense emission lines. The Cu- and Zn-like ions existed in the trap but in smaller concentrations and produced weaker line emission. Appropriately adjusting the beam energy distribution shifted the ion fraction in the trap to ions as low as Kr-like. The experimentally simulated thermal plasmas facilitated the observation of the $5f\rightarrow3d$ transitions in the Kr- to As-like ions. These charge states existed in the plasma with $E_{\mathrm{beam}}=2.66$ keV. However, the $5f\rightarrow3d$ transitions could not be observed in the plasma since the electron beam energy was well below the threshold energy of collisional excitation for these lines. Of course, in the experimentally simulated thermal plasma, the sampled beam energies reached low and high enough to both create ions of these isosequences and to collisionally excite electrons to the $5f$ levels.

Several major emission features exist in the XRS spectra recorded in the beam plasmas. Between ≈2400 eV and a photon energy equivalent to the beam energy, collisionally excited pairs of lines are produced from $nf_{5/2}\rightarrow3d_{3/2}$ and $nf_{7/2}\rightarrow3d_{5/2}$ transitions and $nd_{3/2}\rightarrow3p_{1/2}$ and $nd_{5/2}\rightarrow3p_{3/2}$ transitions (see Figs. 3 and 4) where $n=4$, 5, 6, and 7. The $nf_{5/2}\rightarrow3d_{3/2}$ and $nd_{3/2}\rightarrow3p_{1/2}$ transitions in the Ni- to Kr-like ions are the higher energy component in each pair. Between 1500 and 2400 eV, the emission was dominated by $4s\rightarrow3d$ (electric quadrupole, $E2$), $4p\rightarrow3d$ (electric dipole, $E1$), $4s\rightarrow3p$ ($E1$), $4d\rightarrow3p$ ($E1$), and $4f\rightarrow3p$ ($E2$) transitions. It is interesting to note that the "forbidden" $E2$ transitions were some of the most intense lines in the spectra and were present due to the low density in our experiment. This has been observed before in even higher-Z ions [33,34]. The emission features at photon energies much greater than the line emission were produced by radiative recombination of Ni-like→Cu-like, Cu-like→Zn-like, etc. Line emission be-

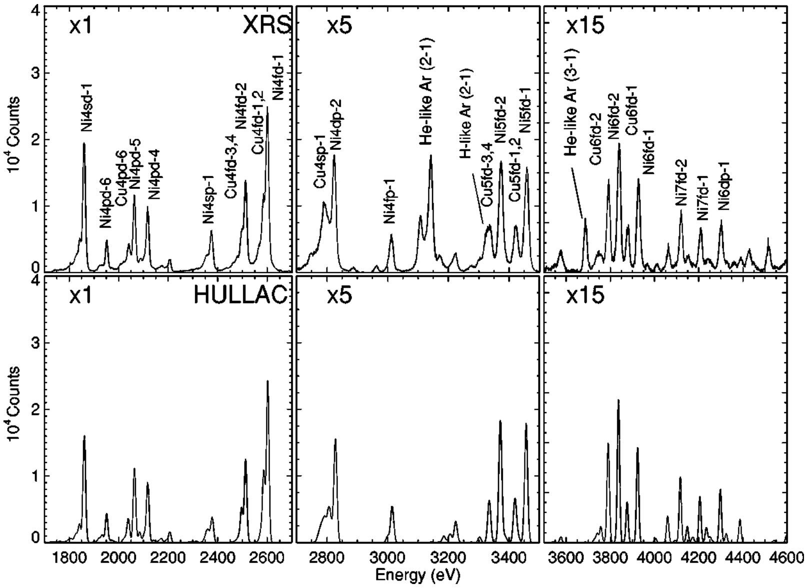

FIG. 6. Photometrically calibrated XRS spectrum of the EBIT-I plasma (top) and synthetic HULLAC spectrum (bottom) at a beam energy of 4.54 keV. $X1$, $X5$, and $X15$ denotes the magnification of the y axis.

tween a photon energy equivalent to the beam energy and the radiative recombination lines were not produced by collisional excitation from the ground. The upper levels of these lines were populated by dielectronic capture channels that were resonant at the beam energy.

The identifications of the $5f\rightarrow 3d$, $4f\rightarrow 3d$, and the Ni4pd-1 transitions measured by the crystal spectrometer are listed in Table I. For most of the lines in the crystal spectra, the identifications were straightforward. Ni-, Zn-, Ge-, and Kr-like ions have closed subshells of $3d^{10}$, $4s^2$, $4p_{1/2}^2$, $4p^6$, respectively. Cu- and Ga-like ions have a single electron in the open $4s$ or $4p_{1/2}$ subshells, respectively, for their ground configurations. These ground configurations resulted in a total of two or four transitions in the $\frac{5}{2}\rightarrow\frac{3}{2}$ and $\frac{7}{2}\rightarrow\frac{5}{2}$ pairs of transitions for each ionization state. For instance, the Ni-like ion had only one line in each pair of $nf_{5/2}\rightarrow 3d_{3/2}$ and $nf_{7/2}\rightarrow 3d_{5/2}$ transitions. The calculated HULLAC x-ray transition energies differed by 3–10 eV from the measured photon energies at 3500 eV. The relative level of accuracy of the calculations was better than in the EUV [18] and was good enough to associate a given measured line to a predicted atomic transition. Unfortunately, a few of the weak $J=\frac{1}{2}\rightarrow\frac{1}{2}$ transitions were blended with the stronger $J=\frac{3}{2}\rightarrow\frac{1}{2}$ transitions and could not be unambiguously identified.

As-, Se-, and Br-like ions have electrons in the open $4p_{3/2}$ subshell, which result in three to four different transitions in each $nf_{5/2}\rightarrow 3d_{3/2}$ and $nf_{7/2}\rightarrow 3d_{5/2}$ line pair that were closely spaced in energy. These lines were weaker than the lines from the adjacent Ge-like ions and were slightly blended in the x-ray crystal spectra, which made their identification less certain. The identification of these lines was done by matching the measured intensities with those from HULLAC. A few of these lines were too weak and could not be identified. Also, the $5f_{7/2}\rightarrow 3d_{5/2}$ transitions of the Br, Se, As, Kr-like ions were very weak since their photon energies were just below the Ar K edge of the proportional counter. Most of these could not be measured. The Ni5pd-1 and Cu4pd-1 transitions were also below the Ar K edge. The XRS photon energies are listed for these two lines.

Identifications and photon energy measurements with the XRS were limited to the more intense transitions of the Ni-, Cu-, Zn-, and Ga-like ions. Detailed identifications of the As- to Kr-like ions could not be done by using the XRS spectra due to its poorer spectral resolution and the large number of relatively weak lines in the spectra.

The line identifications in the XRS spectra were done in a similar manner to the lines in the x-ray crystal spectra. Above 3000 eV, a transition predicted by HULLAC could be associated with a measured line. Below 3000 eV, this was more difficult. Some features were obvious blends of several

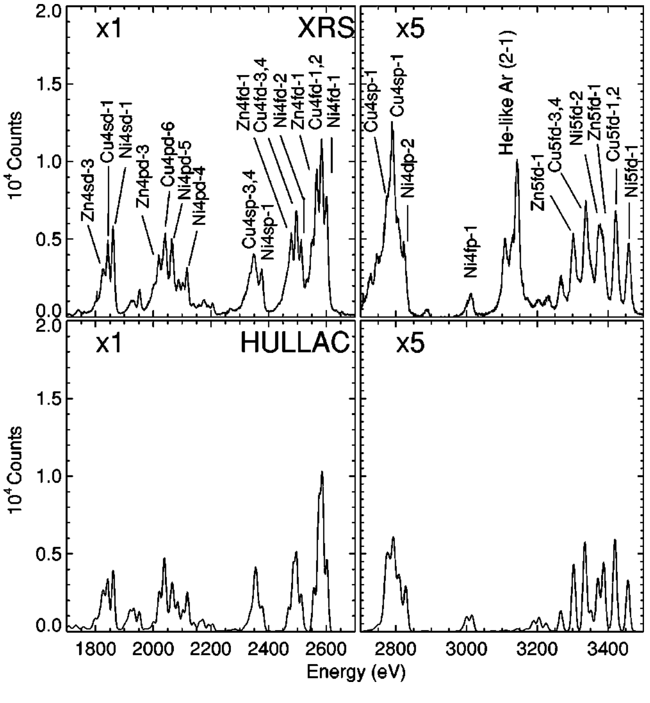

FIG. 7. Photometrically calibrated XRS spectrum of the EBIT-I plasma (top) and synthetic HULLAC spectrum (bottom) at a beam energy of 3.63 keV. *X1* and *X5* denotes the magnification of the y axis.

TABLE III. Comparison of measured and HULLAC line intensities for Ni-, Zn-, and Cu-like Au for a plasma with $E_{\mathrm{beam}}=4.54$ keV for lines with a discrepancy greater than 40% between theory and experiment. Column 1 contains a label given to each line, which includes the isoelectronic sequence, n and ℓ of the upper level, the ℓ of the lower level and a unique number for each line. Errors bars are given in parenthesis. "b" signifies a blended line.

Label	E_{HULLAC} (eV)	$I_{\mathrm{Experiment}}$ (Counts)	I_{HULLAC} (Counts)
Cu4sd-3	1842.23	52000 (200)	23000
Zn4pd-3	2019.77	17000 (100)	3600
Cu4pd-5	2084.60	b	7000
Cu4pd-5	2085.76	21000 (100)	7600
Cu4sd-1	2141.86	6800 (80)	3000
Cu4pd-2	2173.74	9800 (100)	3600
Cu4pd-1	2192.23	6300 (80)	2600
Zn4sp-2	2348.53	b	1100
Zn4sp-2	2354.23	5800 (80)	1400
Cu4sp-3	2361.19	31000 (200)	5100
Cu4sp-3	2362.81	b	5000
Ni4sp-1	2377.58	75000 (300)	26000
Zn4fd-2	2485.09	23000 (200)	7300
Cu4fd-4	2496.40	b	16000
Cu4fd-3	2496.70	66000 (300)	32000
Cu4fd-2	2584.82	b	34000
Cu4fd-1	2586.60	120000 (300)	66000
Zn4sp-1	2772.68	7200 (100)	430
Cu4sp-1	2792.22	23000 (200)	3000
Ni5pd-1	3184.68	6400 (80)	1700
Zn5fd-2	3302.42	4000 (60)	1600
Ni5sp-1	3575.66	2700 (50)	530
Ni5dp-1	3792.55	1900 (40)	5100
Ni7dp-1	4597.86	1400 (40)	640

TABLE IV. Comparison of measured and HULLAC line intensities for Ni-, Zn-, Cu-, and Ga-like Au for a plasma with $E_{\mathrm{beam}}=3.53$ keV for lines with a discrepancy greater than 40% between theory and experiment. Column 1 contains a label given to each line, which includes the isoelectronic sequence, n and ℓ of the upper level, ℓ of the lower level, and a unique number for each line. Errors bars are given in parenthesis. "b" signifies a blended line.

Label	E_{HULLAC} (eV)	$I_{\mathrm{Experiment}}$ (Counts)	I_{HULLAC} (Counts)
Ga4sd-1	1798.34	12000 (100)	5600
Zn4sd-2	1826.92	b	7500
Zn4sd-2	1827.38	45000 (200)	8900
Cu4sd-2	1933.44	12000 (100)	23000
Cu4sp-3	2361.19	48000 (200)	10000
Cu4sp-3	2362.81	b	9400
Ni4sp-1	2377.58	b	10000
Cu4sp-2	2380.73	33000 (200)	14000
Zn4fd-2	2485.09	59000 (200)	76000
Cu4fd-2	2584.82	b	65000
Cu4fd-1	2586.60	120000 (300)	120000
Zn4sp-1	2772.68	17000 (100)	6500
Ga4dp-1	2775.42	b	1500
Ga4dp-1	2776.04	16000 (100)	2900
Cu4sp-1	2792.22	28000 (200)	3200
Zn4dp-1	2794.05	b	11000
Cu4dp-1	3205.60	640 (30)	20
Ni4dp-1	3224.19	1400 (40)	20
Zn5fd-1	3387.14	7300 (90)	17000

lines with a spectral width larger than the instrumental width. More than one HULLAC transition was associated with these features. In some cases, it was not possible to identify individual lines, and all the HULLAC transitions were given the same identification label. For example, five separate HULLAC transitions in the Zn4sd-1 feature could not be individually identified. In a few instances, no measured line could be associated with a predicted HULLAC line.

The emission lines with photon energies greater than $E_{\mathrm{beam}}=3.53$ keV were a result of dielectronic capture of Ni $\rightarrow$Cu-like, Cu$\rightarrow$Zn-like, etc. into states that were resonant at the beam energy. The strongest stabilization transitions were emitted between 3600 and 4000 eV and were fed by capture into states of the form $\overline{3d}3d6\ell n'\ell'$ where $\overline{3d}$ indicates a vacancy in the $3d$ shell and $10\leqslant n'\leqslant 15$. The primary stablization transitions were $3d^{9}6\ell n'\ell'\rightarrow 3d^{10}n'\ell'$. The analysis of the lines fed by dielectronic recombination capture processes will be discussed in a later paper.

VI. SPECTRAL LINE INTENSITIES

Synthetic spectra were generated for the $E_{\mathrm{beam}}=3.53$ and 4.54 keV plasmas. Each intensity was convoluted with a Gaussian line width function with a ΔE_{FWHM} of 12 eV. Figures 6 and 7 compare the photometrically calibrated XRS spectra and the synthetic spectra for both plasmas. The HULLAC spectra have been normalized to the Ni-like $5f\rightarrow 3d$ transitions in the XRS spectra. The features at 3140, 3684, and 3323 eV are the He-like $2p1s\rightarrow 1s^{2}$, He-like $3p1s\rightarrow 1s^{2}$, and the H-like $2p\rightarrow 1s$ transitions of argon and are not modeled here. For both of these plasmas, HULLAC simulated all the features in the XRS spectra and many of the lines' intensities agree within 20–30 %. The agreement is better for the $E_{\mathrm{beam}}=4.54$ keV plasma. The largest disagreement was in the 3.53 keV spectrum at 2600 eV. The $I_{\mathrm{Experiment}}$ and I_{HULLAC} are listed in Tables III and IV for lines where the discrepancy between theory and experiment was greater than 40%. The intensities are the areas of the Gaussians either from the fits or the HULLAC simulations. For blended features, the measured intensity is listed for the brightest feature predicted by HULLAC. The uncertainties on each experimental intensity are just the statistical error. For the weakest lines, the experimental intensity could be greater than the HULLAC prediction by more than a factor of 5.

VII. CONCLUSION

The spectra of Ni- to Kr-like gold have been measured with a crystal spectrometer and an x-ray microcalorimeter in EBIT-I and EBIT-II plasmas having either an experimentally simulated thermal electron distribution of 2.5 keV or a monoenergetic electron beam of 4.54, 3.53, or 2.66 keV. These spectra have been compared with atomic physics calculations from the HULLAC code. Approximately 140 emission lines have been identified and accurate photon energies have been determined. Good agreement exists between the measured and the predicted values of the photon energy for lines between 1500 and 5000 eV. The measured line position may then be used to shift the modeled photon energies. The HULLAC modeling of collisionally excited lines agreed with the spectra recorded by the photometrically calibrated microcalorimeter in the 3.53 and 4.54 keV electron beam plasmas within 20–30 %, although larger differences were noted for some of the weaker lines. This means that the CSD distribution inferred from such comparisons can be off by a similar amount. The present measurements help illustrate the limitations of modern calculations.

ACKNOWLEDGMENT

This work was performed under the auspices of the U.S. Department of Energy by the University of California Lawrence Livermore National Laboratory under Contract No. W-7405-ENG-48.

---

[1] K.L. Wong, P.T. Springer, J.H. Hammer, C.A. Iglesias, A.L. Osterheld, M.E. Foord, H.C. Bruns, and J.A. Emig, Phys. Rev. Lett. **80**, 2334 (1998).

[2] A.L. Velikovich, J. Davis, V.I. Oreshkin, J.P. Apruzese, R.Q. Clark, J.W. Thornhill, and L.I. Rudakov, Phys. Plasmas **8**, 4509 (2001).

[3] C. De Michelis and M. Mattioli, Rep. Prog. Phys. **47**, 1233 (1984).

[4] J.E. Rice, J.L. Terry, K.B. Fournier, M.A. Graf, M. Finkenthal, M.J. May, E.S. Marmar, W.H. Goldstein, and A.E. Hubbard, J. Phys. B **29**, 2191 (1996).

[5] P. Buratti, E. Barbato, G. Bracco, S. Cirant, F. Crisanti, G. Granucci, A.A. Tuccillo, V. Zanza, M. Zerbini, L. Acitelli, F. Alladio, B. Angelini, M.L. Apicella, G. Apruzzese, L. Bertalot, A. Bertocchi, M. Borra, A. Bruschi, G. Buceti, A. Cardinali, C. Centioli, R. Cesario, C. Cianfarani, S. Ciattaglia, V. Cocilovo, R. De Angelis, F. De Marco, B. Esposito, D. Frigione, L. Gabellieri, G. Gatti, E. Giovannozzi, C. Gourlan, M. Grolli, A. Imparato, H. Kroegler, M. Leigheb, L. Lovisetto, G. Maddaluno, G. Maffia, M. Marinucci, G. Mazzitelli, P. Micozzi, F. Mirizzi, S. Nowak, F.P. Orsitto, D. Pacella, L. Panaccione, M. Panella, V. Pericoli Ridolfini, L. Pieroni, S. Podda, G.B. Righetti, F. Romanelli, F. Santini, M. Sassi, S.E. Segre, A. Simonetto, C. Sozzia, S. Sternini, O. Tudisco, V. Vitale, G. Vlad, and F. Zonca, Phys. Rev. Lett. **82**, 560 (1999).

[6] J.C. Raymond and N.C. Brickhouse, Astrophys. Space Sci. **237**, 321 (1996).

[7] H.R. Griem, Phys. Fluids B **4**, 2346 (1992).

[8] M. Fajardo, P. Audebert, P. Renaudin, H. Yashiro, R. Shepherd, J.-C. Gauthier, and C. Chenais-Popovics, Phys. Rev. Lett. **86**, 1231 (2001).

[9] C.Y. Côté, J.C. Kieffer, and O. Peyrusse, Phys. Rev. E **56**, 992 (1997).

[10] S. Kiyokawa, T. Yabe, N. Miyanaga, K. Okada, H. Hasegawa, T. Mochizuki, T. Yamanaka, C. Yamanaka, and T. Kagawa, Phys. Rev. Lett. **54**, 1999 (1985).

[11] C. Bauche-Arnoult, E. Luc-Koenig, J.-F. Wyart, J.-P. Geindre, P. Audebert, P. Monier, J.-C. Gauthier, and C. Chenais-Popovics, Phys. Rev. A **33**, 791 (1986).

[12] M.E. Foord, S.H. Glenzer, R.S. Thoe, K.L. Wong, K.B. Fournier, B.G. Wilson, and P.T. Springer, Phys. Rev. Lett. **85**, 992 (2000).

[13] A. Bar-Shalom, M. Klapisch, and J. Oreg, J. Quant. Spectrosc. Radiat. Transf. **71**, 169 (2001).

[14] S.H. Glenzer, K.B. Fournier, B.G. Wilson, R.W. Lee, and L.J. Suter, Phys. Rev. Lett. **87**, 045002 (2001).

[15] B.G. Wilson *et al.*, *Radiative Properties of Hot Dense Matter*, edited by W. Goldstein, C. Hooper, J. Gauthier, J. Seely, and R. Lee (World Scientific, Singapore, 1991).

[16] M.A. Levine, R.E. Marrs, J.R. Henderson, D.A. Knapp, and M.B. Schneider, Phys. Scr. **22**, 157 (1988).

[17] R. Marrs, P. Beiersdorfer, and D. Schneider, Phys. Today **47**, 27 (1994).

[18] E. Träbert, P. Beiersdorfer, K.B. Fournier, S.B. Utter, and K.L. Wong, Can. J. Phys. **79**, 153162 (2001).

[19] K.L. Wong, M.J. May, P. Beiersdorfer, K.B. Fournier, G.V. Brown, S.B. Utter, and P. Springer, Phys. Rev. Lett. **90**, 235001 (2003).

[20] M.J. May, K.L. Wong, P. Beiersdorfer, B. Wilson, K.B. Fournier, and E. Träbert (unpublished).

[21] F.S. Porter *et al.*, Proc. SPIE **4140**, 407 (2000).

[22] G.V. Brown, P. Beiersdorfer, and K. Widmann, Rev. Sci. Instrum. **70**, 280 (1999).

[23] I.G. Brown, J.E. Galvin, R.A. MacGill, and R.T. Wright, Appl. Phys. Lett. **49**, 1019 (1986).

[24] P. Beiersdorfer, L. Schweikhard, J. Crespo López-Urrutia, and K. Widmann, Rev. Sci. Instrum. **67**, 3818 (1996).

[25] D.W. Savin, P. Beiersdorfer, S.M. Kahn, B.R. Beck, G.V. Brown, M.F. Gu, D.A. Liedahl, and J.H. Scofield, Rev. Sci. Instrum. **71**, 3362 (2000).

[26] R. Kelly *et al.*, Proc. SPIE **3745**, 114 (1999).

[27] K.C. Gendreau *et al.*, Proc. SPIE **3765**, 137 (1999).

[28] M.D. Audley *et al.*, Proc. SPIE **3765**, 751 (1999).

[29] G.W. Drake, Can. J. Phys. **66**, 586 (1988).

[30] J.D. Garcia and J.E. Mack, J. Opt. Soc. Am. **55**, 654 (1963).

[31] K.B. Fournier, M.E. Foord, B.G Wilson, S.H. Glenzer, K.L. Wong, R.S. Thoe, P. Beiersdorfer, and P.T. Springer, in *Atomic Processes in Plasmas*, edited by Kenneth D. Jacobs and R. Coles Sibley III, AIP Conf. Proc. 547 (AIP, NY, 2000).

[32] J. Scofield (private communication).

[33] N. DelGrande, P. Beiersdorfer, J.R. Henderson, A. Osterheld, H. Scofield, and J.K. Swenson, Nucl. Instrum. Methods Phys. Res. B **56/57**, 227 (1991).

[34] P. Beiersdorfer *et al.*, Phys. Rev. Lett. **67**, 2272 (1991).